Pore wall corrugation effect on the dynamics of adsorbed H_2 studied by *in situ* quasi-elastic neutron scattering: Observation of two timescaled diffusion

Miriam Koppel [a], Rasmus Palm [b],[*], Riinu Härmas [a], Margarita Russina [c], Veronika Grzimek [c], Jacek Jagiello [d], Maarja Paalo [a], Heisi Kurig [a], Martin Månsson [b], Ove Oll [a], Enn Lust [a]

[a] *Institute of Chemistry, University of Tartu, Ravila 14a, 50411, Tartu, Estonia*
[b] *Department of Applied Physics, KTH Royal Institute of Technology, SE10691, Stockholm, Sweden*
[c] *Helmholtz-Zentrum Berlin für Materialien und Energie, Hahn-Meitner-Platz 1, 14109, Berlin, Germany*
[d] *Micromeritics Instrument Corporation, 4356 Communications Dr, Norcross, GA, 30093, United States*

ARTICLE INFO

ABSTRACT

The self-diffusion mechanisms for adsorbed H_2 in different porous structures are investigated with *in situ* quasi-elastic neutron scattering method at a temperature range from 50 K to 100 K and at various H_2 loadings. The porous structures of the carbon materials have been characterized by sorption analysis with four different gases and the results are correlated with previous in-depth analysis with small-angle neutron scattering method. Thus, an investigation discussing the effect of pore shape and size on the nature of adsorbed H_2 self-diffusion is performed. It is shown that H_2 adsorbed in nanometer-scale pores is self-diffusing in two distinguishable timescales. The effect of the pore, pore wall shape and corrugation on the fraction of confined and more mobile H_2 is determined and analyzed. The increased corrugation of the pore walls is shown to have a stronger confining effect on the H_2 motions. The difference of self-diffusional properties of the two H_2 components are shown to be smaller when adsorbed in smoother-walled pores. This is attributed to the pore wall corrugation effect on the homogeneity of formed adsorbed layers.

1. Introduction

The self-diffusion of molecular H_2 is strongly linked to the nanoscale molecular transport in carbon materials and hence, is of great interest for many practical applications, such as H_2 storage via physical adsorption, H_2:D_2 separation, and catalysis [1–4]. Neutrons are perfect probes for investigating H_2 diffusion and confinement because H_2 has a large incoherent neutron scattering cross-section. Further, neutrons also have a large penetration depth, enabling the use of complex sample environments and, thus, performing *in situ* measurements [5]. Multiple workgroups have investigated the mass transfer dynamics and nanoscale behaviour of H_2 adsorbed in porous materials with neutron scattering methods [6–15]. However, until now, a majority of such studies have focused on the strong adsorption potential of ultramicropores and micropores through the application of low H_2 loadings prior to measurements. While this allows us to conclude which pores are optimal for the confinement and storage of H_2, it leaves an interpretational gap for the

self-diffusional dynamics of H_2, which is not strongly adsorbed/confined in the ultramicropore and micropore adsorption centers. Thus, an in-depth description and understanding of the less restricted diffusion modes of H_2 in larger pores and at higher loadings are lacking.

In addition to the specific surface area and micropore volume, pore size plays a crucial role in the efficient adsorption of H_2 and other energetically important gases in porous adsorbents [2,7,13,15–18]. Pores with diameters over 15 Å have a small contribution to the H_2 storage capacity, whereas pores in the range from 6 to 7 Å yield the highest H_2 uptake per available surface area at around 1 MPa and 77 K [16,17,19]. More specifically, the interaction strength between the H_2 molecule and the adsorbent pore wall is enhanced in narrow pores (<10 Å) due to adsorbate–adsorbent interaction potential. A potential energy minimum and, thus, a strong confining environment for the H_2 molecule is created, which shifts the sorption equilibrium of H_2 towards adsorption at higher temperature and lower pressure conditions [6,13,15,16]. However, when the distance between H_2 molecule and pore wall

---

becomes even smaller, e.g., $< \sim 3.5$ Å, the binding energy starts to decrease, resulting in reduced confinement [20].

In addition to the pore width, the pore wall corrugation of polycrystalline electrodes, pore surface roughness and shape of carbon materials has been shown both experimentally and theoretically to be an important contributing factor to the confinement of adsorbed H_2 [7, 21–29]. A theoretical study by Konstantakou et al. showed that the surface curvature results in stronger adsorption potential, i.e., the interaction between the adsorbed H_2 and the pore wall is stronger in corrugated pores than in pores with smoother walls [23]. Moreover, it has been shown that carbon adsorbents with prevalently spherical and cylindrical sub-nanometer pores confine H_2 to a larger extent than slit-shaped pores [7]. Significantly different adsorbate density profiles are exhibited upon increased surface coverage (i.e., loading) in corrugated pores and slit-shaped pores [22,30]. This results in adsorption sites with distinctly different adsorption potentials and, thus, different effects on the confinement of adsorbed species.

In corrugated pores, concaves enhance and convexes limit the adsorption potential. Thus, the density of adsorbate in corrugated pores is inhomogeneous at equivalent distances from the pore wall [22, 30–32]. This results in disrupted adsorbate densities and fluctuations in the density beyond the first adsorbed layer on the pore walls, exhibited as clear minima and maxima in the second and further adsorption layer densities [22,30]. However, in pores with smoother walls, the adsorbate density is more homogeneous, and the transitions between adsorbed layers are more ordered [22,30]. The differences of adsorbate densities in pores with different levels of corrugation and between different layers could cause distinguishable self-diffusivities for different adsorbed H_2. Then, the self-diffusional jumps of adsorbed H_2 could occur in timescales that are different enough to be observed experimentally. In this work, we present experimental results which confirm theoretical results [22, 30–32] for the effect of pore wall corrugation on the self-diffusion process.

Carbide-derived carbons (CDCs) have shown excellent performance in a wide range of applications, such as electrode materials in supercapacitors and polymer electrolyte membrane fuel cells, and as adsorbents for H_2 storage applications [28,33–36]. With their highly tunable pore structure, CDCs are excellent model materials to investigate the influence of the porous structure on the adsorption capacity and the strength of interaction between the H_2 and the pore walls [37,38]. Mo_2C derived carbon materials used in this study (denoted as C700, C800 and C900) have been very thoroughly characterized by a wide range of experimental techniques in previous publications, with methods such as small-angle neutron scattering (SANS), small-angle x-ray scattering and *in situ* neutron powder diffraction (NPD) [11,21,38]. It has been established that C700 and C800 exhibit cylindrically shaped pores with higher pore wall corrugation, whereas C900 exhibits prevalently slit-shaped pores with smoother surfaces [21,38]. *In situ* NPD measurements revealed a reversible formation of graphitic domains in C700 and C800 at 50 K and under applied H_2 loadings [11]. The H_2 adsorbed in the ultramicropores of C700 and C800 at low temperatures ($T \leq 20$ K) forms a dense phase, which upon heating to 50 K causes a pressure increase inside the material as the mobility of H_2 molecules increases with increased temperature. The pressure increase is possible because of the locking of H_2 inside the porous carbon structure. The increase in the internal pressure causes a structural change in the adsorbent, i.e., the formation of ordered graphitic regions with three distinct interlayer spacings. When the temperature is increased further, to 60 K, H_2 escapes the porous structure of the material, and the original carbon structure is restored [11]. This phenomenon encouraged the in-depth investigation of the diffusion of H_2 adsorbed in the same materials at various adsorption phases.

The self-diffusion of H_2 adsorbed in C700, C800, and C900 is probed using the *in situ* quasi-elastic neutron scattering (QENS) method. We have investigated the self-diffusion of weakly adsorbed H_2 in the temperature range of 50–100 K and H_2 loading pressures range of 0.1–10 bar

to obtain deeper knowledge about the diffusional processes in the same materials. The deconvolution of the H_2 jump diffusion at different timescales provides valuable insight into the presence of multilayer H_2 adsorption and the nature of adsorbed layer formation process while adsorbed at higher H_2 loadings in pores with different shapes.

2. Materials and methods

2.1. Synthesis of the Mo_2C derived carbon adsorbents

A more detailed description of the synthesis of the CDC samples is given elsewhere [37]. Briefly, Mo_2C (99.5%, −325 mesh powder, Sigma-Aldrich) was placed onto a quartz stationary bed and synthesized by chlorination at reaction temperatures 700 °C, 800 °C and 900 °C for 4.5 h. The samples are denoted according to their chlorination temperatures in °C as C700, C800, and C900. The reaction equation is as follows (Eq. (1)):

$$Mo_2C + 2Cl_2 \rightarrow C + 2MoCl_2 \qquad (1)$$
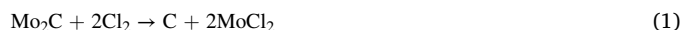
The residual chlorine, chlorides, oxygen-containing functional groups etc., were removed from the surface of the CDC with H_2 gas mixture applied at 900 °C for 1 h.

2.2. Gas adsorption measurements

N_2, Ar, CO_2, and H_2 isotherms of all three CDC samples were measured with ASAP 2020 (Micromeritics, USA) at 77 K, 87 K, 273 K, and 77 K, respectively. Before the measurements, the samples were outgassed at 300 °C and 13 μbar for 12 h.

The pore size distributions were calculated with SAIEUS (Micromeritics, USA) software (developmental version) by applying the two-dimensional non-local density functional theory model for carbon materials with heterogeneous surfaces (2D-NLDFT-HS) simultaneously to N_2, Ar, CO_2 and H_2 adsorption isotherm data [39]. The 2D-NLDFT-HS model fitting results are presented in the SI in section 11. Specific surface area, S_{DFT}, and volume of pores, V_{DFT}, were calculated by applying the 2D-NLDFT-HS model. Including the H_2 adsorption isotherm data extends the lower limit of pore size distribution analysis below that of standard N_2 or CO_2 measurements [40]. More specifically, H_2 molecules can access, in comparison to N_2 molecules, pores smaller than 0.7 nm that are not always probed by N_2 but play a significant role in the uptake and confinement of H_2 [40].

2.3. Quasi-elastic neutron scattering (QENS) experiment

The neutron scattering data were collected using the time-of-flight spectrometer NEAT'2016 at the neutron source BER II in Helmholtz Zentrum Berlin (HZB), Germany [41,42]. The average incident neutron wavelength $\lambda_i \approx 5$ Å ($E_i \sim 3.3$ meV) resulted in neutron detection in the momentum transfer range, $Q \approx 0.3$ to 2.4 Å^{-1} and energy resolution, $\Delta E \approx 100$ μeV. The Q range was truncated because of the coherent scattering occurring due to the (002) Bragg peak from graphitic carbon with a maximum at $2\theta \sim 26°$, corresponding to ~ 1.8 Å^{-1}. At $Q < \sim 0.55$ Å^{-1}, the signal was relatively noisy and the deconvolution of the elastic and quasi-elastic components was not reliable. Initial data reduction and background subtraction routines were performed using the Mantid software package [43]. Scattering data binning was performed in three different Q ranges (from 0.2 to 2.45 Å^{-1}, from 0.25 to 2.5 Å^{-1}, and from 0.3 to 2.4 Å^{-1} with a step of 0.15 Å^{-1}) and in two different E ranges (from −2 to 2 meV, at low loading pressures, and from −3 to 2 meV, at medium and high loading pressures, with a step of 8 μeV). The binned scattering data is available at https://doi.org/10.23673/re-324.

Before the QENS measurement, all three CDCs were outgassed for > 17 h at > 250 °C to remove moisture and other adsorbed species. After the outgassing process, the CDCs were transferred into a double-walled

cylindrical aluminum sample holder with an outer diameter of 1.02 cm and an inner diameter of 0.555 cm. Sample handling and preparation were performed in a glovebox filled with inert gas.

The measurement protocol for all three CDCs was identical and is detailed in SI of Ref. [11]. The signal from the vanadium cell and the empty sample holder was measured for detector normalization and background subtraction. The experiments with the three CDC samples were conducted as follows:

1. The signal from outgassed CDCs was measured at 20 K, 50 K, 60 K, 70 K, 80 K, 90 K, and 100 K.
2. The samples were cooled down to 77 K and H_2 was dosed in the sample holder until the pressure reached the p_{H2load} value in Table 1. The adsorption equilibrium was established in approximately 1 h.
3. The sample holder was disconnected from the gas dosing apparatus and the CDCs containing H_2 were measured at different temperatures ranging from 20 K to 100 K, i.e., the same temperature series as for the outgassed CDC. After each temperature change, the system was let to reach an equilibrium during approximately 40 min before the start of the scattering measurement. C700 was also measured at 30 K and 40 K at $p_{H2,load} = 68$ mbar.

Steps 2.-3. Were repeated for two other $p_{H2,load}$ values. Data from the outgassed samples were subtracted from the dynamic structure factors of the sample containing H_2, which yielded the dynamic structure factor originating only from H_2, $S_{H2}(Q,E)$ (Fig. 1a). The $p_{H2,load}$ values were chosen so that a filling of ultramicropores, micropores and additionally mesopores would be achieved at lowest, medium, and highest applied $p_{H2,load}$, respectively. Thus, the influence of different sized pores on the transport properties of adsorbed H_2 is probed at the chosen $p_{H2,load}$ values.

The $p_{H2,load}$ and the corresponding amounts of H_2 in the sample cell (n_{H2}) can be seen in Table 1. The $p_{H2,load}$ calculations were made based on the assumption that smaller pores are filled first [44] and can be seen in more detail in SI sections 1 and 2. Throughout the entire experiment, the pressure in the sample cell, p_{H2}, was monitored and the amount of adsorbed H_2 and pore occupancies were calculated at different $p_{H2,load}$ and temperature conditions based on the measured p_{H2} value (Table S1).

2.3.1. The detection and separation of the diffusion occurring at two different time scales

The broadening of the quasi-elastic component is obtained by fitting the $S_{H2}(Q,E)$ with Eq. (2) (Fig. 1a). The $S_{H2}(Q,E)$ obtained under low $p_{H2,load}$ is fitted with a model containing one quasi-elastic component described with one Lorentzian function (Fig. 1b and Eq. (2), where $n = 1$):

$$S_{H2}(\boldsymbol{Q}, E) = A_0(\boldsymbol{Q})\delta(E) + \sum_{i}^{n} A_i(\boldsymbol{Q})L(E, \Gamma_i), \qquad (2)$$

where $S_{H2}(\boldsymbol{Q},E)$ is the dynamical structure factor of adsorbed H_2, $\boldsymbol{Q}$ is the scattering vector, E is the energy transfer, $\delta(E)$ is the Dirac delta function describing the elastic scattering, A_0 is the fraction of elastic scattering signal, A_n is the fraction of quasi-elastic scattering signal, where n is the number of quasi-elastic components and where $A_0 + \sum_{i=1}^{n} A_i = 1$, L is the

Table 1
H_2 loading pressures ($p_{H2,load}$) at 77 K and the corresponding total amount of H_2 per 1 g of CDC (n_{H2}) in the closed sample cell.

	Lowest H_2 loading		Medium H_2 loading		Highest H_2 loading	
	$p_{H2,load}$ mbar	n_{H2} mmol g^{-1}	$p_{H2,load}$ mbar	n_{H2} mmol g^{-1}	$p_{H2,load}$ mbar	n_{H2} mmol g^{-1}
C700	68	4	1047	21	10 028	125
C800	86	4	1056	21	9972	138
C900	86	3	1017	18	10 193	121

Lorentzian function which describes the quasi-elastic component mathematically, and Γ is the half-width at half maximum (HWHM) of the quasi-elastic component.

The $S_{H2}(Q,E)$ at $p_{H2,load} = 1$ bar and $p_{H2,load} = 10$ bar are fitted with a model containing two quasi-elastic components described with two Lorentzian functions (Eq. (2), where $n = 2$; Fig. 1c) to confirm the presence of and to investigate H_2 mobility in two distinguishable time-scales. However, at $p_{H2,load} = 1$ bar and at $T = 50$ K, the narrower of the two quasi-elastic components could not be reliably deconvoluted (SI section 4) and thus, is fitted with a model containing one Lorentzian function (Eq. (2), where $n = 1$). The $S_{H2}(Q,E)$ measured at $p_{H2,load} = 10$ bar are fitted with a model containing two Lorentzian functions (Eq. (2), where $n = 2$) throughout the entire T range.

2.3.2. Calculation of diffusivity parameters

The translational diffusion dynamics of H_2 can be described by modeling the obtained Γ vs Q dependence with a translational jump-diffusion model [5,45]. The translational jump-diffusion models proposed by Hall-Ross [46] (Eq. (3)) and Singwi-Sjölander [47] (Eq. (5)) consider deviations from continuous diffusion described by Fick's law at larger Q values through limiting values of jump lengths, which is caused by the porous structure of the adsorbent. Hall-Ross model (Eq. (3)) assumes that the jump lengths follow a Gaussian distribution (Eq. (4)), which describes jump diffusion in a restricted volume, e.g., narrow pores.

$$\Gamma_{HR}(Q) = \frac{\hbar}{\tau}\left(1 - \exp\left(-Q^2\tau D\right)\right) \qquad (3)$$

$$\rho_{HR}(l) = \frac{2l^2}{l_0^3\sqrt{2\pi}}\exp\left(-\frac{l^2}{2l_0^2}\right) \qquad (4)$$

where $\Gamma(Q)$ is the half-width at half maximum of the quasi-elastic component at a given Q value and HR denotes the Hall-Ross model, $\hbar$ is the reduced Planck constant, τ is the residency time, D is the diffusion coefficient, $\rho(l)$ is the distribution of jump lengths, l is the mean jump length, and l_0 is the distribution mode value, where $l^2 = 3l_0^2$ and $l = \sqrt{6tD}$.

The model proposed by Singwi and Sjölander, originally developed for liquid water (Eq. (5)), is based on exponential jump length distribution (Eq. (6)) and characterizes diffusion which alternates between oscillatory and directed motions [47].

$$\Gamma_{SS}(Q) = \frac{\hbar D Q^2}{1 + D Q^2 \tau} \qquad (5)$$

$$\rho_{SS}(l) = \frac{l}{l_0^2}\exp\left(-\frac{l}{l_0}\right) \qquad (6)$$

where SS denotes Singwi-Sjölander model, $l^2 = 6l_0^2$, and $l = \sqrt{D\tau}$.

The fitting results can be seen in SI in sections 6-9. An Arrhenius-type equation can be used to describe the temperature dependency of diffusion coefficients of H_2 adsorbed in porous carbons (Eq. (7)) [6,7]. By applying this relation, the activation energy of the diffusion process, E_a, and the extrapolated diffusion coefficient at infinite temperature, D_0, can be calculated from the slope and intercept of the graph, respectively.

$$D = D_0 \exp\left(-\frac{E_a}{RT}\right) \qquad (7)$$

where D is the diffusion coefficient, R is the universal gas constant, and T is the temperature.
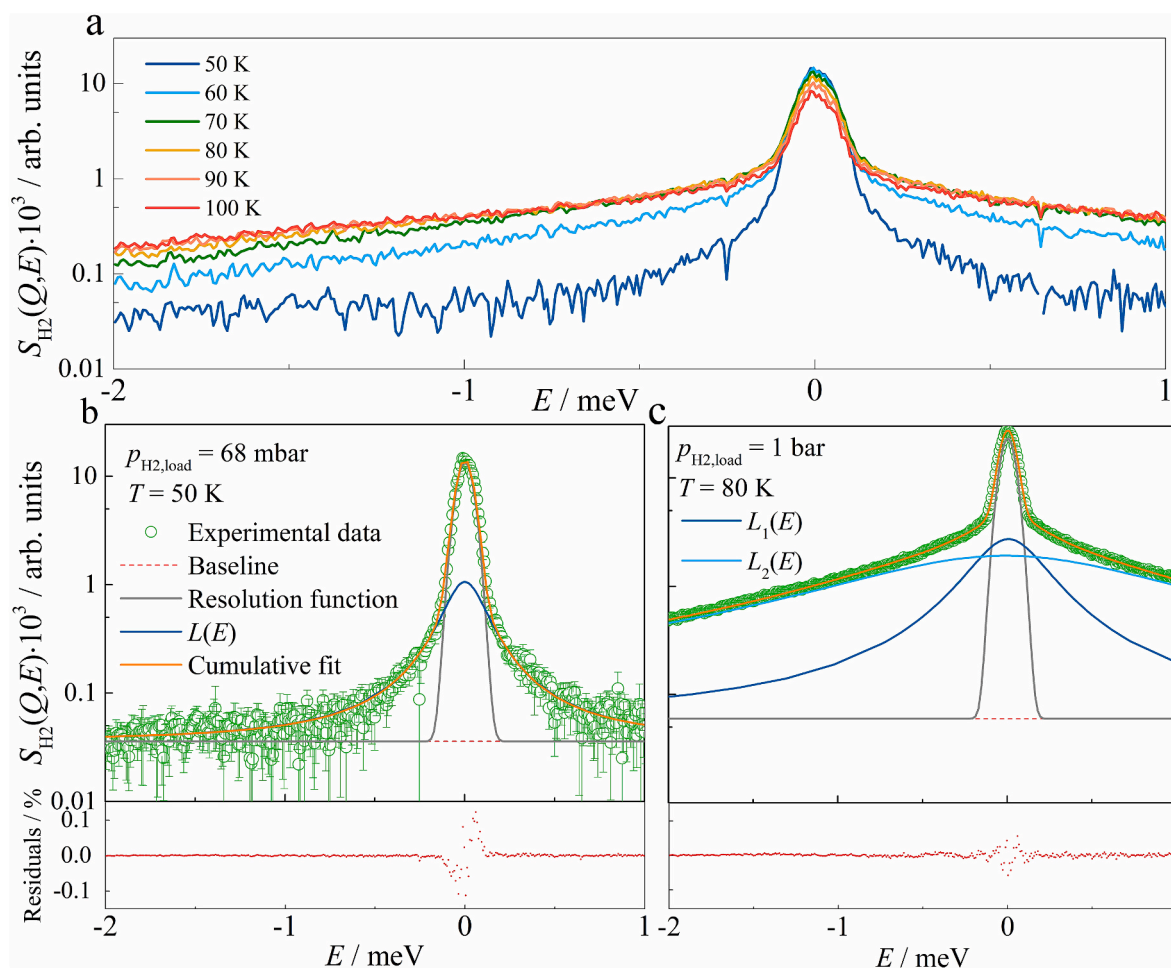
Fig. 1. The $S_{H2}(Q,E)$ of C700 at $Q = 0.875$ Å^{-1} at a) T-s 50–100 K, b) at $T = 50$ K at $p_{H2,load} = 68$ mbar fitted with one quasi-elastic component mathematically described with one Lorentzian function, $L(E)$, and c) at 80 K at $p_{H2,load} = 1$ bar fitted with two quasi-elastic components mathematically described with two Lorentzian functions, $L_1(E)$ and $L_2(E)$, (Eq. (2)), plotted with residual values below. (A colour version of this figure can be viewed online.)

3. Results and discussion

3.1. Ultramicropores and pore wall corrugation

The simultaneous application of the 2D-NLDFT-HS model on the N$_2$, Ar, CO$_2$, and H$_2$ gas adsorption data reveals that a higher chlorination temperature will lead to a decrease in the specific surface area, S_{DFT}, and pore volume, V_{DFT}, of the CDC (Fig. 2, inset) as previously also established in Refs. [21,24,37].

The pore size distributions have been previously calculated for the same CDCs on three different occasions by applying the 2D-NLDFT-HS model simultaneously to the N$_2$ and CO$_2$ adsorption data [7], to the Ar and CO$_2$ adsorption data [21] and only to the N$_2$ adsorption data [37]. The pore size distributions modeled in Refs. [7,21,37] are bimodal, with the first maximum corresponding to pores with widths smaller than 20 Å (micropores) and the second maximum corresponding to pores with widths larger than 20 Å (mesopores). Including the H$_2$ adsorption data and applying the 2D-NLDFT-HS model simultaneously to N$_2$, Ar, CO$_2$, and H$_2$ adsorption data, as in Fig. 2, extends the lower analysis limit of the obtained pore size distribution down to the ultramicropore range, pore widths < 7 Å, and gives a more realistic picture of the porous structure [48,49]. Thus, trimodal pore size distributions are obtained (Fig. 2), where the first maximum corresponds to pores in the ultramicropore range, with pore widths < 7 Å, which have a crucial role in the storage and confinement of H$_2$ [6].

Ultramicropores can be interpreted as the measure of corrugation/

roughness of the pore walls. Thus, a larger volume of ultramicropores in C700 and C800 than in C900 indicates that the micro- and mesopores of C700 and C800 exhibit higher degree of pore wall corrugation than C900. This corroborates with the contrast matched SANS study on the same materials in Ref. [21], which revealed that with the increase in synthesis temperature, the surface roughness of pore walls decreases.

3.2. H$_2$ adsorption and diffusion at the lowest H$_2$ loading pressure

At the lowest $p_{H2,load}$, approximately 7% of the available pore volume is filled with H$_2$ at 50 K in case of all investigated CDC materials, assuming that the density of adsorbed H$_2$ is equal to that of liquid H$_2$ (70.85 g dm^{-3}). Ultramicropores are filled predominantly at the lowest $p_{H2,load}$, as the smallest pores have been shown to fill first (Fig. 3a and b) [44,50]. H$_2$ is strongly confined in the ultramicropores of the samples at $T \leq 50$ K since the measured p_{H2} value at 50 K in the sample cell ($p_{H2} \leq 0.0023$ bar) indicates almost no H$_2$ is present in the free volume (Fig. 3c and d, Tables S1 and S5, and in Ref. [11]). Knowing the p_{H2} values at all experimental instances and the integrated areas of the quasi-elastic and elastic components enables us to calculate the estimated fractions of gaseous phase (desorbed), mobile and immobile H$_2$ molecules, respectively, shown in Fig. 3c and d.

At 50 K, approximately 70–80% of H$_2$ molecules adsorbed in the CDC are fixed, i.e., immobile in the experimental timescale (Fig. 3c and d) (C800 is presented in SI Fig. S11). This supports the pore occupancy calculations, based on which a large fraction of H$_2$ molecules are
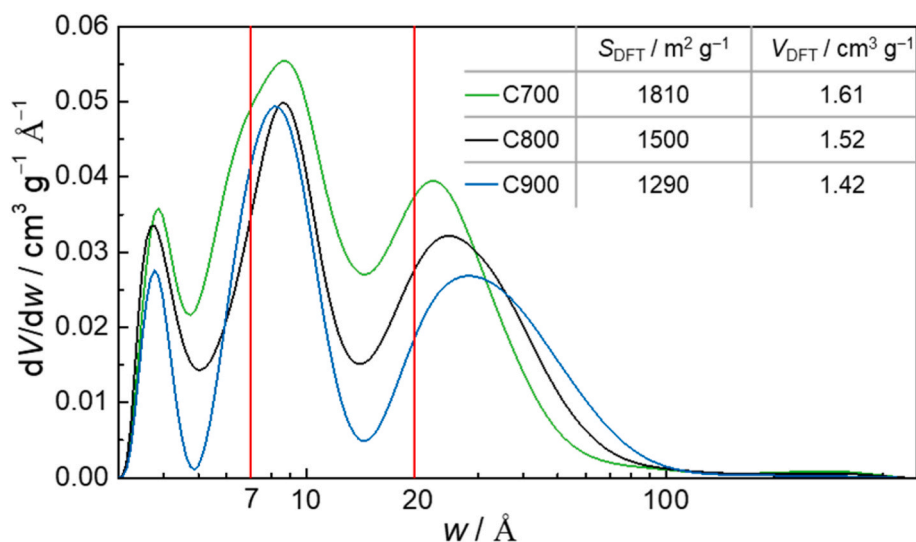
Fig. 2. The trimodal pore size distribution by differential pore volume calculated by simultaneously applying 2D-NLDFT-HS model to the N_2, Ar, CO_2, and H_2 adsorption data and the corresponding specific surface areas, S_{DFT}, and pore volumes, V_{DFT}, in the inset. Red lines denote the limits of ultramicro- and micropores. (A colour version of this figure can be viewed online.)
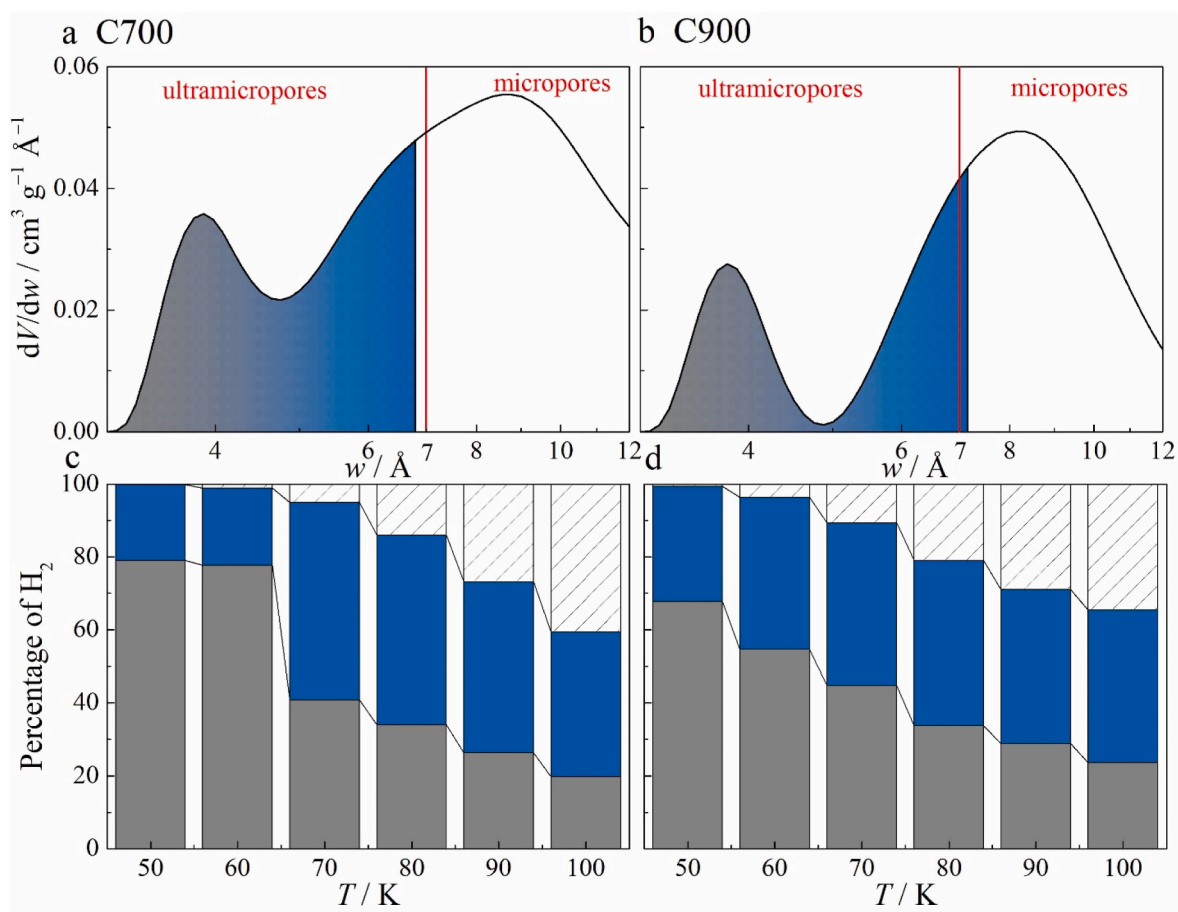
Fig. 3. Pore size distributions of a) C700 and b) C900 plotted with the corresponding pore occupancy at $T = 50$ K (filled area under the curve); the red vertical line denotes the limit of ultramicropores. Estimated percentages of gaseous phase (hatched), mobile (blue) and fixed (gray) H_2 from the total H_2 present in the sample cell under the lowest $p_{H2,load}$ for c) C700 and d) C900 are obtained at $Q = 0.875$ Å^{-1} and $Q = 0.85$ Å^{-1}, respectively. (A colour version of this figure can be viewed online.)

adsorbed in the ultramicropores which strongly confine H_2 at higher temperature and lower pressure conditions [6]. In C700, a change from 60 K to 70 K results in a more rapid increase in the amount of mobile H_2 than in the case of C900 (Fig. 3c and d). In addition, the absolute amount

of immobile H_2 in C700 is larger than in C900 (Table S10 in SI). Thus, the porous structure of C700 has a more enhanced capability to confine adsorbed H_2 than C900 due to the larger volume of ultramicropores present in C700.

As the temperature increases onward and some of the H_2 desorbs and diffuses out of the CDCs into the gas phase, the fraction of the mobile part reaches a more-or-less consistent value at $T > 70$ K with a fraction of $\sim 30\%$ of H_2 immobile (Fig. 3c and d; C800 can be seen in Fig. S11). Thus, the fixed component is most likely the H_2 which is adsorbed strongly in the ultramicropores, and the mobile component is H_2 adsorbed in larger ultramicro- and micropores, yielding lower confinement.

It is evident that with the increase in T, the H_2 jump length distributions become wider as kinetic energy of H_2 becomes larger and long jumps become less restricted (Fig. 4a). With increased T, more H_2 is desorbed from the pores as in Fig. 3c, the density of H_2 in the pores decreases and therefore, the diffusion of H_2 left in the pores is less restricted (similar effect is investigated in Ref. [51]). The jump length distributions of H_2 adsorbed in C700 and C800 at 50 K are notably narrower than the jump length distributions of H_2 at temperatures ≥ 60 K, indicating that the mobility of adsorbed H_2 is very restricted at 50 K. This restricted mobility of H_2 adsorbed in C700 and C800 at $T = 50$ K has been previously analyzed through the D value of adsorbed H_2 in Ref. [11]. The jump length distribution of H_2 adsorbed in C900 does not depend on the applied T, compared to C800 and C700, as H_2 is not as well confined in the larger pores and porous structure of C900 (Fig. 4b).

Although the pore width is defined as the linear distance between opposing pore walls, the jump distance of H_2 adsorbed in the pore can be larger than the pore width when the H_2 molecule performs jumps along the pore wall or diagonally inside the pore. The pore occupancy calculations and pore size distributions indicate that at least in the case of C900, H_2 was also adsorbed in pores wider than 7 Å at 50 K (Fig. 3b). Thus, at least at $T \leq 50$ K, H_2 adsorption was not limited only to the ultramicropores but also to micropores. Even at 100 K, the jumps of H_2 adsorbed in CDC-s are restricted to ~ 20 Å (Fig. 4), confirming that micropores, additionally to ultramicropores, restrict the diffusion of adsorbed H_2.

3.3. Diffusion of adsorbed H_2 in two timescales[1]

Higher H_2 loadings of $p_{H2,load} = 1$ bar and $p_{H2,load} = 10$ bar were applied to confirm the presence of adsorbed H_2 transport at different timescales, where multilayer adsorption of H_2 in larger pores could be related with increased mobility of adsorbed H_2. Approximately 30% of all the available pore volume of the samples is filled with H_2 at $p_{H2,load} = 1$ bar and at 50 K. At $T \leq 50$ K, pressure readings in the sample cell indicate low pressure ($p \leq 0.4$ bar), similarly to measurements at lowest $p_{H2,load}$. An estimation of the pore occupancy indicates that at 50 K, H_2 is adsorbed in ultramicropores and micropores. At $p_{H2,load} = 10$ bar, the amount of the adsorbed H_2 is the highest, and at 50 K, H_2 is adsorbed in most pores (see SI section 2 for details).

At increased pressures and low temperatures, the density of adsorbed H_2 inside ultramicro- and micropores of carbon samples is higher than that of the bulk liquid phase [29,52,53]. This is most likely the cause for the strong confinement of adsorbed H_2 (almost 60% immobile and only 4% in the gas phase) and only one detectable self-diffusional timescale (Fig. 5a) for adsorbed H_2 at $p_{H2,load} = 1$ bar and at $T = 50$ K.

The self-diffusion in two timescales can be interpreted as the separable self-diffusion of H_2 adsorbed closer to the pore wall and H_2 adsorbed in multilayers, i.e., in the middle region of the pore, and their hindrance can be expressed through self-diffusion E_a. The logarithmic self-diffusion coefficients are linear with respect to the inverse value of T and thus, Arrhenius relation can be applied to calculate the E_a-s (Fig. 6a). The fraction of H_2 adsorbed closer to the pore wall has a considerably higher translational jump activation energy, E_a, and the

fraction of H_2 with lower E_a values is adsorbed farther from the pore wall (Fig. 6b).

For C700, at $p_{H2,load} = 10$ bar and at the low temperature of 50 K, approximately half of the H_2 inside the sample cell is in gaseous phase and the other half is adsorbed in most pores of the CDC (Fig. 5b). Almost half of the adsorbed H_2 at 50 K is immobile, corresponding to ~ 30 mmol g^{-1} of H_2 (the absolute values of immobile H_2 can be seen in Table S10). A relatively large amount of immobile H_2 can be explained by the formation of a dense H_2 phase inside ultramicro- and micropores, similarly as in the case of $p_{H2,load} = 1$ bar, where ~ 13 mmol g^{-1} of H_2 is immobile. Surprisingly, even at a high temperature of 100 K, when most of the H_2 is in the gaseous phase or has high mobility, approximately 5% of H_2 is effectively immobile. This corresponds to ~ 7 mmol g^{-1} of immobile H_2.

The increase of $p_{H2,load}$ from 86 mbar to 1 bar results in increase in E_a values, which are attributed to H_2 being adsorbed with a relatively higher density, resulting in intermolecular hindrance and restricting the self-diffusional motions. The E_a values of both slower and faster H_2 components adsorbed in more corrugated pores of C700 are higher than in smoother-walled pores of C900 at $p_{H2,load} = 1$ bar and at $p_{H2,load} = 86$ mbar (Fig. 6b), indicating a higher degree of H_2 confinement in C700. The increased corrugation of the pore walls of C700 indicated by the larger volume of ultramicropores (Fig. 2) enables the increase of the effective adsorption potential, resulting in enhanced interaction strength, which has previously been shown theoretically in Refs. [22, 30–32]. This causes restrictions in the diffusion process resulting in higher E_a values for H_2 adsorbed in more corrugated pores of C700 than in pores with smoother walls, as in C900.

When H_2 is adsorbed in C900 at $p_{H2,load} = 1$ bar, the smoother pore walls (indicated by the lower volume of ultramicropores) have less effect on the diffusion hindrance of different components of adsorbed H_2 indicated by the similar E_a values (blue columns in Fig. 6b). Thus, although the self-diffusion of H_2 still occurred clearly in two different timescales in C900 (Fig. S7d), the calculated E_a-s for these diffusion modes were nevertheless similar. The layering of adsorbed H_2 in the more corrugated pores of C700 is disrupted – some fraction of H_2 is adsorbed at equivalent distance from pore wall but with varying density profiles. These regions of different H_2 densities cause different E_a-s for H_2 self-diffusion since E_a will be higher if the molecules restrict each other's movement in the regions with higher density. In conclusion, higher pore corrugation leads to larger difference in the density of H_2 in different regions of the pore, which in turn leads to larger difference in the E_a of self-diffusion of H_2. Thus, at 1 bar, the E_a of the slower and faster self-diffusion of H_2 in C700 are markedly more different from each other than the E_a of the slower and faster self-diffusion of H_2 in C900.

Even at $p_{H2,load} = 10$ bar, there is still an adsorbed H_2 component for which motions are restricted, indicated by the relatively high E_a values (Fig. 6b), in addition to the considerable fraction of fixed H_2 (Fig. 5b). The amount of immobile and adsorbed H_2 increases severalfold with the increase of $p_{H2,load}$ from 1 bar to 10 bar (Tables S10 and S11), even though the fraction of immobile H_2 decreases with higher $p_{H2,load}$ (Fig. 5). This confirms a previous observation that even at the highest $p_{H2,load} = 10$ bar, there is a fraction of adsorbed H_2 for which self-diffusion is highly hindered. The fraction of H_2 with highly restricted self-diffusion is most likely the H_2 component adsorbed and confined in the micropores and in the concaves of the micropores, i.e. ultramicropores.

The amplified confining effect on H_2 of the more corrugated pores, present in case of C700, is not evident at the highest $p_{H2,load} = 10$ bar. This is indicated by the E_a values of the slower H_2 components, which are of similar value for all investigated CDCs (Fig. 6b; results for C800 can be seen in SI section 10). However, the E_a values of the faster moving component show that at $p_{H2,load} = 10$ bar, a considerable amount of H_2 is weakly interacting with the adsorbent and the adsorbed H_2 layers and, thus, is self-diffusing with virtually no restrictions at all, which limits the capability to analyse the faster H_2 component at the highest H_2 loading

---

[1] C800 will be excluded from the presented analysis onward since C700 and C800 exhibit very similar relations compared to the results from C900. The detailed series of results, including C800, is presented within the SI.
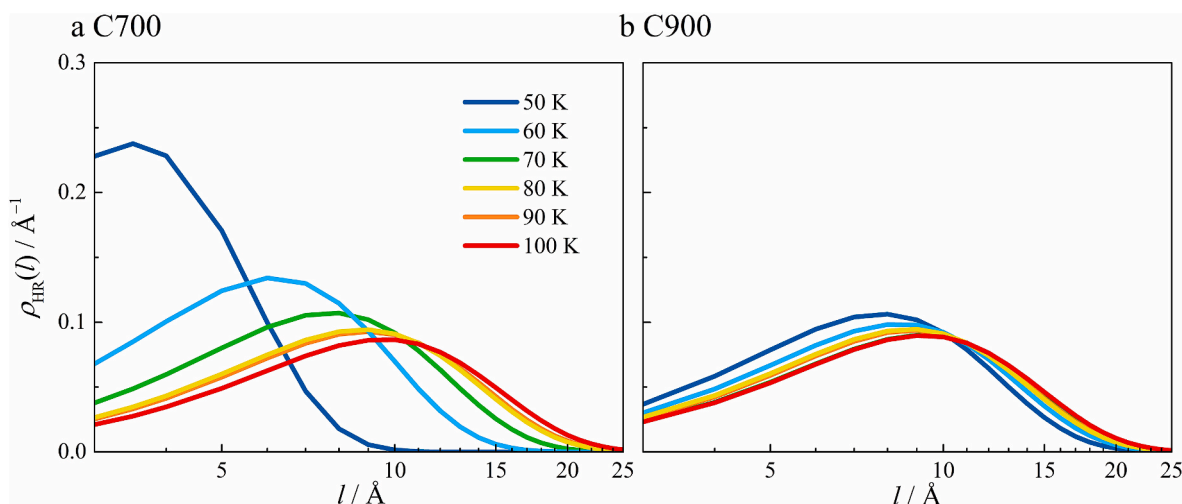
Fig. 4. Jump length distributions calculated according to the Hall-Ross equation from the mobile fraction of H_2 adsorbed in the ultramicropores of a) C700 and b) C900 in the T range from 50 K to 100 K (Eq. (4)) at the lowest applied $p_{H2,load}$. (A colour version of this figure can be viewed online.)
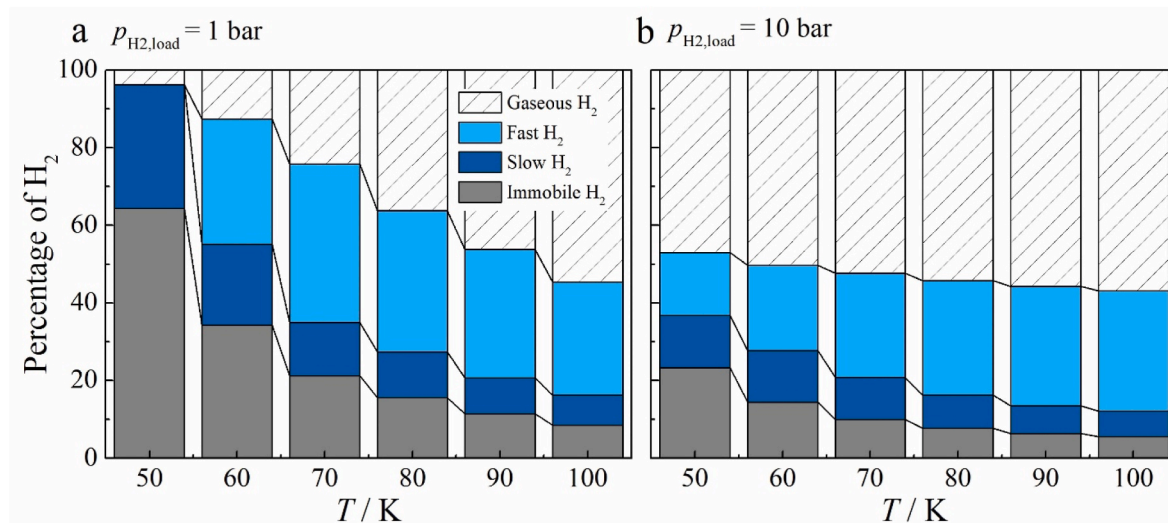
Fig. 5. The percentage of gas-phase (hatched) and adsorbed (colored) H_2 in the closed sample cell. The percentage of mobile (denoted with blue, where darker and lighter tones denote slower and faster H_2 diffusion, respectively) and fixed (denoted with gray) H_2 adsorbed in C700 obtained at $Q = 0.875$ Å^{-1} and at a) $p_{H2,load} = 1$ bar and b) $p_{H2,load} = 10$ bar. Analogous graphs for C800 and C900 can be seen in SI (SI Fig. S12). (A colour version of this figure can be viewed online.)

pressure. However, the very high mobility of the faster component is especially evident from the considerably higher D values at $p_{H2,load} = 10$ bar (Fig. S9c).

4. Conclusion

The self-diffusion of adsorbed H_2 at two timescales in porous carbons with different porous structures is investigated with *in situ* QENS method at a wide range of temperatures and H_2 loading pressures. The pore size distribution of the carbons is very thoroughly characterized using the gas adsorption method with four different gases, which extends the lower limit of pore size distribution analysis below that of standard measurements. The gas adsorption analysis revealed that with the decrease in synthesis temperature of the samples, the volume of ultra-micropores increases, evidencing the increase in the roughness/corrugation of the walls of micro- and mesopores. The change in pore wall corrugation with the synthesis temperature was also previously seen in a contrast matched SANS experiment [21].

From the neutron scattering data, at higher H_2 loadings, where H_2

occupies micro- and mesopores and has more freedom of mobility, clear evidence of H_2 self-diffusion at two different timescales is obtained. The H_2 molecules exhibiting slower and faster self-diffusion are interpreted as the ones adsorbed closer and farther from the pore wall, respectively. More corrugated pores (evidenced by the larger volume of ultra-micropores) result in the increased hindrance of adsorbed H_2 motions which is reflected in the higher values of self-diffusion E_a-s of C700 and C800 compared to C900. In addition, the difference in the E_a of self-diffusion of H_2 diffusing in the same carbon, but with significantly different self-diffusion coefficient, is much larger in the more corrugated pores of C700 as opposed to C900. This is explained by the in-homogeneity in the density of the adsorbed H_2 layers in more corrugated pores. Even at the highest applied H_2 loading ($p_{H2,load} = 10$ bar), motions of a fraction of the adsorbed H_2 molecules are strongly hindered and are effectively immobile. The absolute amount of immobile and adsorbed H_2 increases with increased H_2 loading pressure, although the percentage of immobile and/or adsorbed H_2 in the closed sample cell decreases with the increase of H_2 loading pressure.
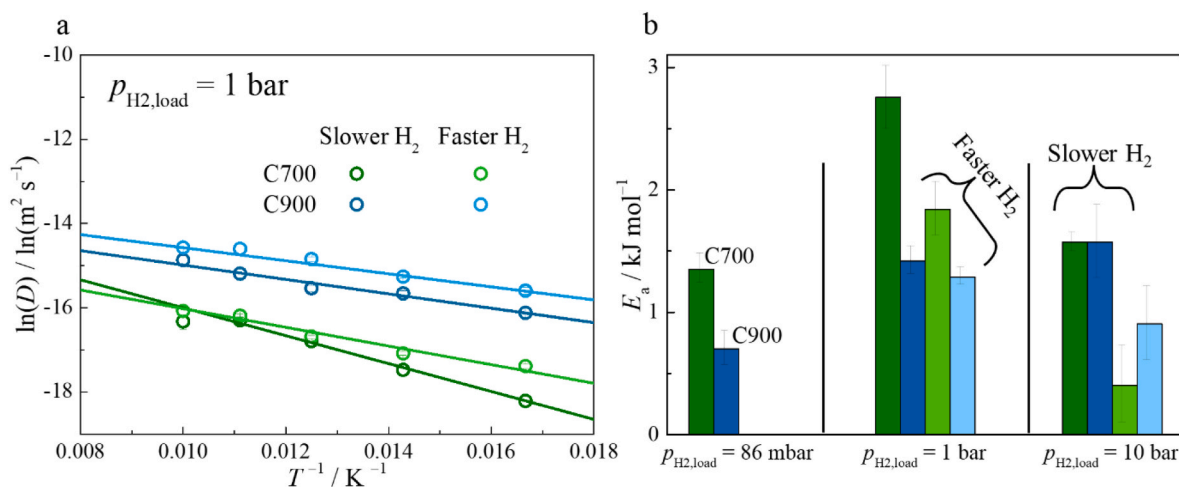
Fig. 6. a) Arrhenius-type plot at $p_{H2,load} = 1$ bar fitted with Arrhenius equation (solid lines, Eq. (7)) (other $p_{H2,load}$-s shown in SI in section 10), where T^{-1} in the inverse value of temperature (error bars are brought inside the symbols) and b) the jump activation energies (E_a) calculated from the Arrhenius-type plots at different $p_{H2,load}$ values for C700 (green bars) and C900 (blue bars) in case of slower (darker tones) and faster (lighter tones) H_2 diffusional components. (A colour version of this figure can be viewed online.)

CRediT authorship contribution statement

Miriam Koppel: Conceptualization, Formal analysis, Investigation, Writing – original draft, Visualization. **Rasmus Palm:** Conceptualization, Formal analysis, Investigation, Writing – original draft. **Riinu Härmas:** Conceptualization, Writing – review & editing. **Margarita Russina:** Formal analysis, Validation, Writing – review & editing. **Veronika Grzimek:** Formal analysis. **Jacek Jagiello:** Formal analysis, Validation. **Maarja Paalo:** Resources. **Heisi Kurig:** Conceptualization, Investigation, Supervision. **Martin Månsson:** Supervision, Writing – review & editing. **Ove Oll:** Investigation. **Enn Lust:** Supervision, Writing – review & editing.

Declaration of competing interest

The authors declare that they have no known competing financial interests or personal relationships that could have appeared to influence the work reported in this paper.

Acknowledgements

Appendix A. Supplementary data

Supplementary data to this article can be found online at https://doi.org/10.1016/j.carbon.2022.06.061.

References

[1] E. Masika, R. Mokaya, Hydrogen storage in high surface area carbons with identical surface areas but different pore sizes: direct demonstration of the effects of pore size, J. Phys. Chem. C 116 (2012) 25734–25740, https://doi.org/10.1021/jp3100365.

[2] Y. Xia, Z. Yang, Y. Zhu, Porous carbon-based materials for hydrogen storage: advancement and challenges, J. Mater. Chem. A. 1 (2013) 9365–9381, https://doi.org/10.1039/C3TA10583K.

[3] M.G. Nijkamp, J.E.M.J. Raaymakers, A.J. van Dillen, K.P. de Jong, Hydrogen storage using physisorption – materials demands, Appl Phys A 72 (2001) 619–623, https://doi.org/10.1007/s003390100847.

[4] R. Jäger, P.E. Kasatkin, E. Härk, E. Lust, Oxygen reduction on molybdenum carbide derived micromesoporous carbon electrode in alkaline solution, Electrochem. Commun. 35 (2013) 97–99, https://doi.org/10.1016/j.elecom.2013.08.001.

[5] M. Bee, Quasielastic Neutron Scattering, Adam Hilger, United Kingdom, 1988.

[6] C.I. Contescu, D. Saha, N.C. Gallego, E. Mamontov, A.I. Kolesnikov, V.V. Bhat, Restricted dynamics of molecular hydrogen confined in activated carbon nanopores, Carbon 50 (2012) 1071–1082, https://doi.org/10.1016/j.carbon.2011.10.016.

[7] R. Härmas, R. Palm, M. Russina, H. Kurig, V. Grzimek, E. Härk, et al., Transport properties of H_2 confined in carbide-derived carbons with different pore shapes and sizes, Carbon 155 (2019) 122–128, https://doi.org/10.1016/j.carbon.2019.08.041.

[8] E. Bahn, O. Czakkel, B. Nagy, K. László, S. Villar-Rodil, J.M.D. Tascón, et al., Diffusion of molecular hydrogen in carbon aerogel, Carbon 98 (2016) 572–581, https://doi.org/10.1016/j.carbon.2015.11.034.

[9] E. Bahn, L.A. Hoyos Giraldo, V. Kuznetsov, I. Calvo-Almazán, M. Zbiri, M.M. Koza, et al., Ultra-fast diffusion of hydrogen in a novel mesoporous N-doped carbon, Carbon 166 (2020) 307–315, https://doi.org/10.1016/j.carbon.2020.05.004.

[10] J. Bahadur, C.I. Contescu, A.J. Ramirez-Cuesta, E. Mamontov, N.C. Gallego, Y. Cheng, L.L. Daemen, et al., Properties of immobile hydrogen confined in microporous carbon, Carbon 117 (2017) 383–392, https://doi.org/10.1016/j.carbon.2017.03.007.

[11] M. Koppel, R. Palm, R. Härmas, M. Russina, N. Matsubara, M. Månsson, et al., *In situ* observation of pressure modulated reversible structural changes in the graphitic domains of carbide-derived carbons, Carbon 174 (2021) 190–200, https://doi.org/10.1016/j.carbon.2020.12.025.

[12] Y. Yang, C.M. Brown, C. Zhao, A.L. Chaffee, B. Nick, D. Zhao, et al., Micro-channel development and hydrogen adsorption properties in templated microporous carbons containing platinum nanoparticles, Carbon 49 (2011) 1305–1317, https://doi.org/10.1016/j.carbon.2010.11.050.

[13] M.-C. Schlegel, D. Többens, R. Svetogorov, M. Krüger, N. Stock, H. Reinsch, et al., Conformation-controlled hydrogen storage in the CAU-1 metal–organic framework, Phys. Chem. Chem. Phys. 18 (2016) 29258–29267, https://doi.org/10.1039/C6CP05310F.

[14] M. Jung, J. Park, R. Muhammad, J.Y. Kim, V. Grzimek, M. Russina, et al., Elucidation of diffusivity of hydrogen isotopes in flexible MOFs by quasi-elastic neutron scattering, Adv. Mater. 33 (2021), 2007412, https://doi.org/10.1002/adma.202007412.

[15] M. Russina, E. Kemner, F. Mezei, Intra-cage dynamics of molecular hydrogen confined in cages of two different dimensions of clathrate hydrates, Sci. Rep. 6 (2016), 27417, https://doi.org/10.1038/srep27417.

[16] G. Sdanghi, R.L.S. Canevesi, A. Celzard, M. Thommes, V. Fierro, C, in: Characterization of Carbon Materials for Hydrogen Storage and Compression, vol. 6, 2020, p. 46, https://doi.org/10.3390/c6030046.

[17] Y. Gogotsi, C. Portet, S. Osswald, J.M. Simmons, T. Yildirim, G. Laudisio, et al., Importance of pore size in high-pressure hydrogen storage by porous carbons, Int. J. Hydrogen Energy 34 (2009) 6314–6319, https://doi.org/10.1016/j.ijhydene.2009.05.073.

[18] R. Palm, I. Tallo, T. Romann, H. Kurig, Methane adsorption on specially designed TiC and Mo₂C derived carbons with different pore size and surface morphology, Micropor. Mesopor. Mater. 218 (2015) 167–173, https://doi.org/10.1016/j.micromeso.2015.07.016.

[19] H.S. Kim, J.P. Singer, Y. Gogotsi, J.E. Fischer, Molybdenum carbide-derived carbon for hydrogen storage, Microporous Mesoporous Mater. 120 (2009) 267–271, https://doi.org/10.1016/j.micromeso.2008.11.019.

[20] P.A. Georgiev, D.K. Ross, P. Albers, A.J. Ramirez-Cuesta, The rotational and translational dynamics of molecular hydrogen physisorbed in activated carbon: a direct probe of microporosity and hydrogen storage performance, Carbon 44 (2006) 2724–2738.

[21] R. Palm, R. Härmas, E. Härk, B. Kent, H. Kurig, M. Koppel, et al., Study of the structural curvature in Mo₂C derived carbons with contrast matched small-angle neutron scattering, Carbon 171 (2021) 695–703, https://doi.org/10.1016/j.carbon.2020.09.070.

[22] J. Jagiello, J. Kenvin, Consistency of carbon nanopore characteristics derived from adsorption of simple gases and 2D-NLDFT models. Advantages of using adsorption isotherms of oxygen (O₂) at 77 K, J. Colloid Interface Sci. 542 (2019) 151–158, https://doi.org/10.1016/j.jcis.2019.01.116.

[23] M. Konstantakou, A. Gotzias, M. Kainourgiakis, A.K. Stubos, T.A. Steriotis, GCMC Simulations of Gas Adsorption in Carbon Pore Structures, IntechOpen, 2011, https://doi.org/10.5772/15988.

[24] H. Kurig, M. Russina, I. Tallo, M. Siebenbürger, T. Romann, E. Lust, The suitability of infinite slit-shaped pore model to describe the pores in highly porous carbon materials, Carbon 100 (2016) 617–624, https://doi.org/10.1016/j.carbon.2016.01.061.

[25] M. Eikerling, A.A. Kornyshev, E. Lust, Optimized structure of nanoporous carbon-based double-layer capacitors, J. Electrochem. Soc. 152 (2005) E24–E33, https://doi.org/10.1149/1.1825379.

[26] L.I. Daikhin, A.A. Kornyshev, M. Urbakh, Nonlinear Poisson–Boltzmann theory of a double layer at a rough metal/electrolyte interface: a new look at the capacitance data on solid electrodes, J. Chem. Phys. 108 (1998) 1715–1723, https://doi.org/10.1063/1.475543.

[27] E. Lust, A. Jänes, V. Sammelselg, P. Miidla, K. Lust, Surface roughness of bismuth, antimony and cadmium electrodes, Electrochim. Acta 44 (1998) 373–383, https://doi.org/10.1016/S0013-4686(98)00084-X.

[28] T. Thomberg, A. Jänes, E. Lust, Energy and power performance of electrochemical double-layer capacitors based on molybdenum carbide derived carbon, Electrochim. Acta 55 (2010) 3138–3143, https://doi.org/10.1016/j.electacta.2010.01.075.

[29] M. Tian, M.J. Lennox, A.J. O'Malley, A.J. Porter, B. Krüner, S. Rudić, et al., Effect of pore geometry on ultra-densified hydrogen in microporous carbons, Carbon 173 (2021) 968–979, https://doi.org/10.1016/j.carbon.2020.11.063.

[30] J. Jagiello, J.P. Olivier, 2D-NLDFT adsorption models for carbon slit-shaped pores with surface energetical heterogeneity and geometrical corrugation, Carbon 55 (2013) 70–80, https://doi.org/10.1016/j.carbon.2012.12.011.

[31] B. Kuchta, L. Firlej, M. Marzec, P. Boulet, Microscopic mechanism of adsorption in cylindrical nanopores with heterogenous wall structure, Langmuir 24 (2008) 4013–4019, https://doi.org/10.1021/la704017u.

[32] J. Jagiello, J. Kenvin, C.O. Ania, J.B. Parra, A. Celzard, V. Fierro, Exploiting the adsorption of simple gases O₂ and H₂ with minimal quadrupole moments for the dual gas characterization of nanoporous carbons using 2D-NLDFT models, Carbon 160 (2020) 164–175, https://doi.org/10.1016/j.carbon.2020.01.013.

[33] E. Härk, S. Sepp, P. Valk, K. Vaarmets, J. Nerut, R. Jäger, et al., Impact of the various catalysts (Pt, Pt-Ru) deposited onto carbon support to the slow oxygen reduction reaction kinetics, ECS Trans. 45 (2013) 1–11, https://doi.org/10.1149/04521.0001ecst.

[34] T. Thomberg, A. Jänes, E. Lust, Energy and power performance of vanadium carbide derived carbon electrode materials for supercapacitors, J. Electroanal. Chem. 630 (2009) 55–62, https://doi.org/10.1016/j.jelechem.2009.02.015.

[35] T. Tooming, T. Thomberg, H. Kurig, A. Jänes, E. Lust, High power density supercapacitors based on the carbon dioxide activated carbon electrodes and 1-ethyl-3-methylimidazolium tetrafluoroborate ionic liquid, J. Power Sources 280 (2015) 667–677, https://doi.org/10.1016/j.jpowsour.2015.01.157.

[36] L. Naheed, M. Koppel, M. Paalo, K. Alsabawi, K.E. Lamb, E. MacA. Gray, et al., Hydrogen adsorption properties of carbide-derived carbons at ambient temperature and high pressure, Int. J. Hydrogen Energy 46 (2021) 15761–15772, https://doi.org/10.1016/j.ijhydene.2021.02.109.

[37] A. Jänes, T. Thomberg, H. Kurig, E. Lust, Nanoscale fine-tuning of porosity of carbide-derived carbon prepared from molybdenum carbide, Carbon 47 (2009) 23–29, https://doi.org/10.1016/j.carbon.2008.07.010.

[38] E. Härk, A. Petzold, G. Goerigk, S. Risse, I. Tallo, R. Härmas, et al., Carbide derived carbons investigated by small angle X-ray scattering: inner surface and porosity vs. graphitization, Carbon 146 (2019) 284–292, https://doi.org/10.1016/j.carbon.2019.01.076.

[39] J. Jagiello, Stable numerical solution of the adsorption integral equation using splines, Langmuir 10 (1994) 2778–2785, https://doi.org/10.1021/la00020a045.

[40] J. Jagiello, C.O. Ania, J.B. Parra, L. Jagiello, J.J. Pis, Using DFT analysis of adsorption data of multiple gases including H₂ for the comprehensive characterization of microporous carbons, Carbon 45 (2007) 1066–1071, https://doi.org/10.1016/j.carbon.2006.12.011.

[41] M. Russina, G. Guenther, V. Grzimek, R. Gainov, M.-C. Schlegel, L. Drescher, et al., Upgrade project NEAT'2016 at Helmholtz Zentrum Berlin – what can be done on the medium power neutron source, Phys. B Condens. Matter 551 (2018) 506–511, https://doi.org/10.1016/j.physb.2017.12.026.

[42] G. Günther, M. Russina, Background optimization for the neutron time-of-flight spectrometer NEAT, Nucl. Instrum. Methods Phys. Res. Sect. A Accel. Spectrom. Detect. Assoc. Equip. 828 (2016) 250–261, https://doi.org/10.1016/j.nima.2016.05.022.

[43] O. Arnold, J.C. Bilheux, J.M. Borreguero, A. Buts, S.I. Campbell, L. Chapon, et al., Mantid—data analysis and visualization package for neutron scattering and μ SR experiments, in: Nuclear Instruments and Methods in Physics Research. Section A, Accelerators, Spectrometers, Detectors and Associated Equipment, 2014, p. 764, https://doi.org/10.1016/j.nima.2014.07.029.

[44] B. Schmitz, U. Müller, N. Trukhan, M. Schubert, G. Férey, M. Hirscher, Heat of adsorption for hydrogen in microporous high-surface-area materials, ChemPhysChem 9 (2008) 2181–2184, https://doi.org/10.1002/cphc.200800463.

[45] R. Hempelmann, Quasielastic Neutron Scattering and Solid State Diffusion, Clarendon Press, 2000.

[46] P.L. Hall, D.K. Ross, Incoherent neutron scattering functions for random jump diffusion in bounded and infinite media, Mol. Phys. 42 (1981) 673–682, https://doi.org/10.1080/00268978100100521.

[47] K.S. Singwi, A. Sjölander, Diffusive motions in water and cold neutron scattering, Phys. Rev. 119 (1960) 863–871, https://doi.org/10.1103/PhysRev.119.863.

[48] J. Jagiello, W. Betz, Characterization of pore structure of carbon molecular sieves using DFT analysis of Ar and H₂ adsorption data, Microporous Mesoporous Mater. 108 (2008) 117–122, https://doi.org/10.1016/j.micromeso.2007.03.035.

[49] L.S. Blankenship, J. Jagiello, R. Mokaya, Confirmation of pore formation mechanisms in biochars and activated carbons by dual isotherm analysis, Mater. Adv (2022), https://doi.org/10.1039/D2MA00141A.

[50] S. Mascotto, J.C. Kuzmicz, D. Wallacher, M. Siebenbürger, D. Clemens, S. Risse, et al., Poly(ionic liquid)-derived nanoporous carbon analyzed by combination of gas physisorption and small-angle neutron scattering, Carbon 82 (2015) 425–435, https://doi.org/10.1016/j.carbon.2014.10.086.

[51] J.H. Petropoulos, A.I. Liapis, N.P. Kolliopoulos, J.K. Petrou, N.K. Kanellopoulos, Restricted diffusion of molecules in porous affinity chromatography adsorbents, Bioseparation 1 (1990) 69–88.

[52] J. Rogacka, L. Firlej, B. Kuchta, Modeling of low temperature adsorption of hydrogen in carbon nanopores, J. Mol. Model. 23 (2017) 20, https://doi.org/10.1007/s00894-016-3202-y.

[53] V.P. Ting, A.J. Ramirez-Cuesta, N. Bimbo, J.E. Sharpe, A. Noguera-Diaz, V. Presser, et al., Direct evidence for solid-like hydrogen in a nanoporous carbon hydrogen storage material at supercritical temperatures, ACS Nano 9 (2015) 8249–8254, https://doi.org/10.1021/acsnano.5b02623.